Supplementary Information

Liquid crystal phase of counter-rotating staircases – A case of antiferrochirality

Ya-xin Li[1,2], Hong-fei Gao[3], Rui-bin Zhang[2], Kutlwano Gabana[4], Qing Chang[3], Gillian A. Gehring[4], Xiao-hong Cheng[3,5]*, Xiang-bing Zeng[2]* and Goran Ungar[1,2]*

1. State Key Laboratory for Mechanical Behaviour of Materials, Shaanxi International Research Centre for Soft Matter, Xi'an Jiaotong University, Xi'an, 710049, P. R. China. Email: g.ungar@xjtu.edu.cn; g.ungar@sheffield.ac.uk
2. Department of Materials Science and Engineering, University of Sheffield, Sheffield S1 3JD, UK. E-mail: x.zeng@sheffield.ac.uk
3. Key Laboratory of Medicinal Chemistry from Natural Resources, Ministry of Education, Yunnan University, Kunming, P. R. China
4. Department of Physics and Astronomy, University of Sheffield, Sheffield E1 2C, UK
5. School of Chemistry and Chemical Engineering, Yangtze Normal University, Fuling, P. R. China. E-mail: xhcheng@ynu.edu.cn

Table of Contents

S1. DSC thermograms

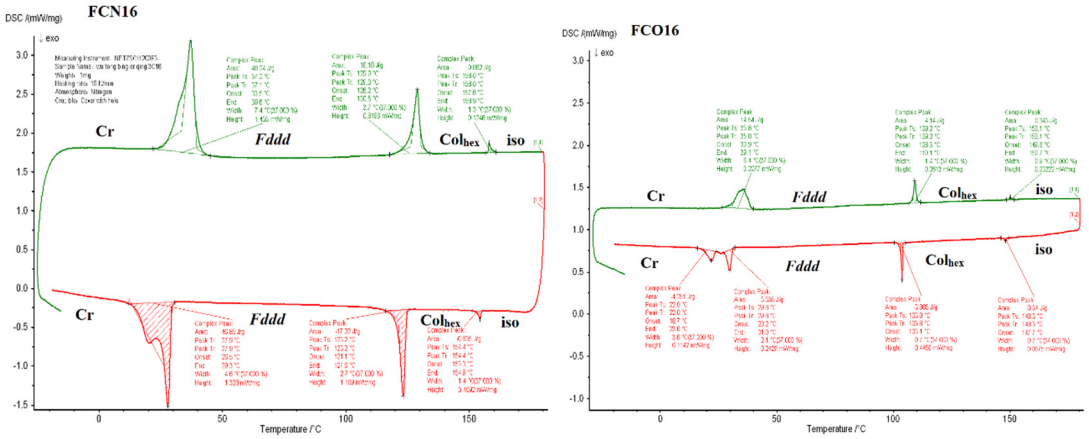

Supplementary Fig. S1 DSC heat flow thermograms (endo up) of compounds **FCN16 and FO16** at heating and cooling scan rate of 10 K min^{-1}.

S2. Polarized optical microscopy (POM)

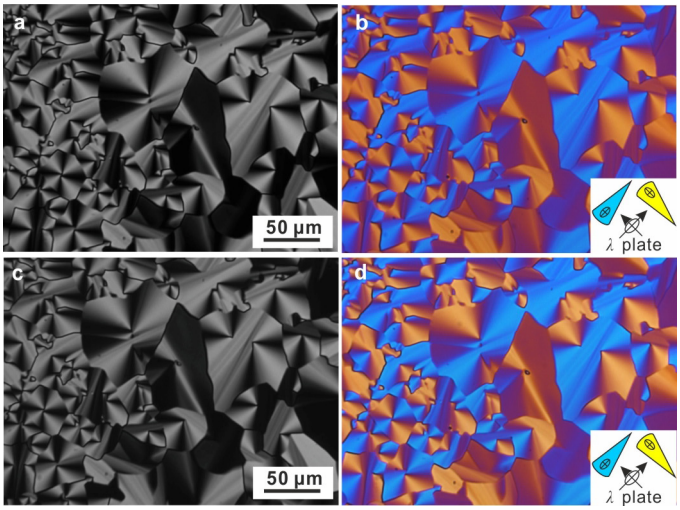

Supplementary Fig. S2 POM of **IC^3/14** examined at **a**, **b** 70 ºC and **c**, **d** 40 ºC, at which temperatures the sample was in Col and *Fddd* phases, respectively. (**b**, **d**) are recorded with a full-wave (λ) plate.

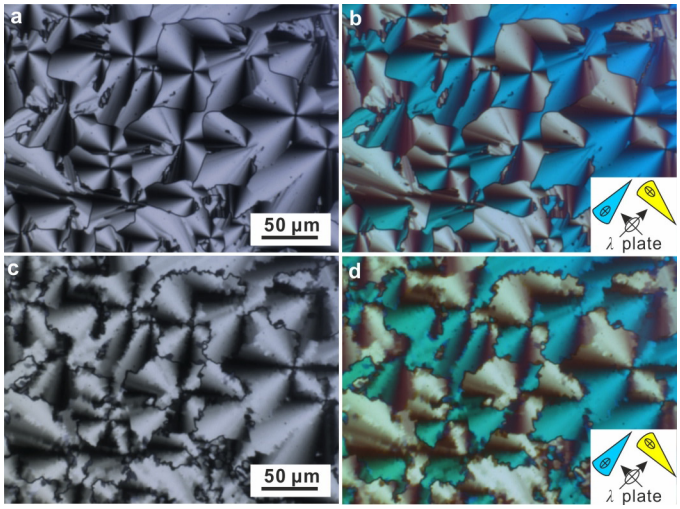

Supplementary Fig. S3 POM of **FCN16** examined at **a**, **b** 140 ºC and **c**, **d** 100 ºC, at which temperatures the sample was in Col and *Fddd* phases, respectively. (b, d) are recorded with a full-wave (λ) plate.

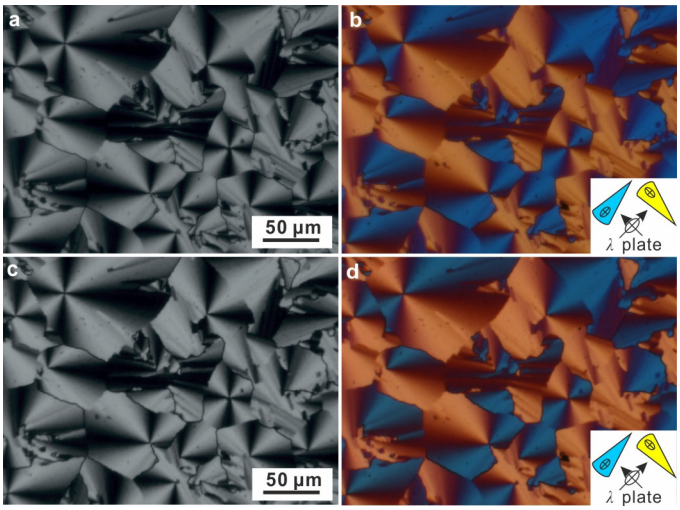

Supplementary Fig. S4 POM of **FO16** examined at (a,b) 140 ºC and (c, d) 90 ºC, at which temperatures the sample was in Col and *Fddd* phases, respectively. (b, d) are recorded with a full-wave (λ) plate.

S3. X-ray diffraction data

IC^3/12

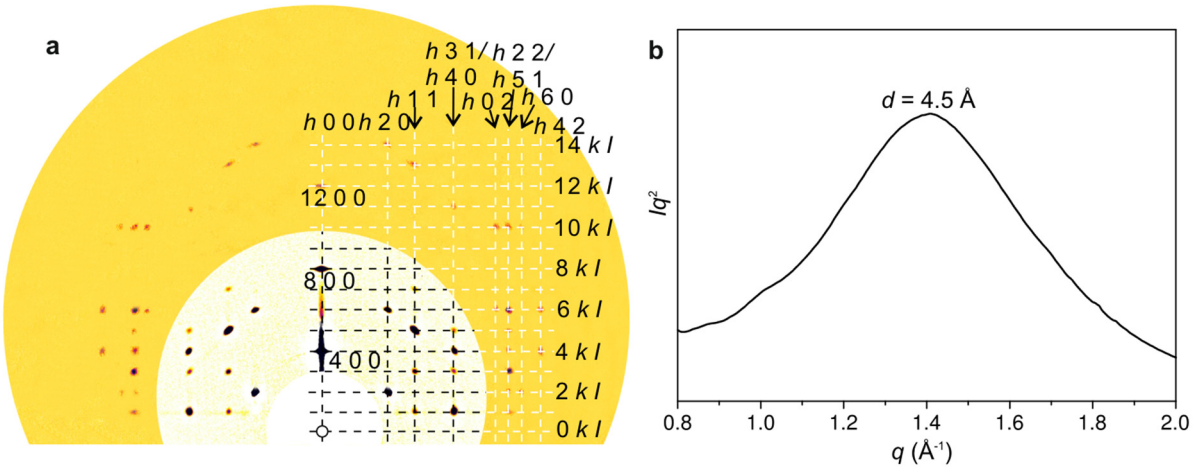

Supplementary Fig. S5 a, GISAXS pattern and **b**, transmission powder WAXS curve of *Fddd* phase of **IC^3/12** recorded at 60 ºC. Fitted background has been subtracted separately from the inner (white) and outer (yellow) portions of the GISAXS pattern.

Supplementary Table S1 Indices, experimental, calculated *d*-spacings, intensities, phases and lattice parameters of diffraction peaks of **IC^3/12** recorded by transmission powder SAXS in the *Fddd* phase at 60 °C. All intensities are Lorentz and multiplicity corrected.

(*hkl*)	experimental *d*-spacings (Å)	calculated *d*-spacings (Å)	*Intensity*	*Phase*
(220)	45.2	45.3	93.0	0
(400)	43.3	43.4	100.0	π
(111)	37.2	37.2	0.4	-
(311)	31.7	31.8	0.4	-
(131)	26.4	26.4	4.0	-
(511)[a] (620)	25.6	25.6	6.4 3.8	0 -
(331)	24.3	24.3	0.2	-
(440)	26.8	26.3	3.9	-
(800)	21.7	21.7	1.2	-
(531)	21.2	21.2	0.1	-
(711)	20.8	20.8	0.1	-
a = 173.5 Å, b = 106.1 Å and c = 40.8 Å				

a: (511) and (620) diffraction peaks are overlapping in the powder diffraction pattern. While their total intensity is taken from the powder diffraction curve, the intensity ratio between the two has been determined from the GISAXS pattern. An azimuthal scan through the (511) and (620) diffraction peaks in the 2D GISAXS pattern is obtained first, and the intensities of the two diffraction peaks are measured from the areas of the diffraction peaks in the scan by fitting each peak to a Gaussian function. Due to the sample geometry, equivalent to a fibre pattern (multiple domains sharing the same *a*-axis), measured intensities needed to be multiplied by the corresponding q_{yz}, i.e. q vector component which is perpendicular to the common *a*-axis of the domains. For (511) and (620) these are $q_{(011)}$ and $q_{(020)}$ respectively. Further correction by diffraction peak multiplicity leads to an intensity ratio $I_{(511)}$: $I_{(620)}$ of 63:37.

Supplementary Table S2 Reflection conditions and space groups.

Reflection conditions							Space group
hkl	*h*0*l*	*hk*0	0*kl*	*h*00	0*k*0	00*l*	
h + *k*, *h* + *l*, *k* + *l*	*h* + *l*	*h* + *k*	*k* + *l*	*h*	*k*	*l*	*F*222, *Fmm*2, *Fm*2*m*, *F*2*mm*, *Fmmm*,
	h, *l*	*h* + *k* = 4n; *h*, *k*	*k* + *l* = 4n; *k*, *l*	*h* = 4n	*k* = 4n	*l* = 4n	*Fd*2*d*
	h + *l* = 4n; *h*, *l*	*h*, *k*	*k* + *l* = 4n; *k*, *l*	*h* = 4n	*k* = 4n	*l* = 4n	*Fdd*2
	h + *l* = 4n; *h*, *l*	*h* + *k* = 4n; *h*, *k*	*k*, *l*	*h* = 4n	*k* = 4n	*l* = 4n	*F*2*dd*
	h + *l* = 4n; *h*, *l*	*h* + *k* = 4n; *h*, *k*	*k* + *l* = 4n; *k*, *l*	*h* = 4n	*k* = 4n	*l* = 4n	*Fddd*

* *h* + *k* means the value of *h* + *k* is even; *h*, *k* and *l* means the values are even.

IC^3/14

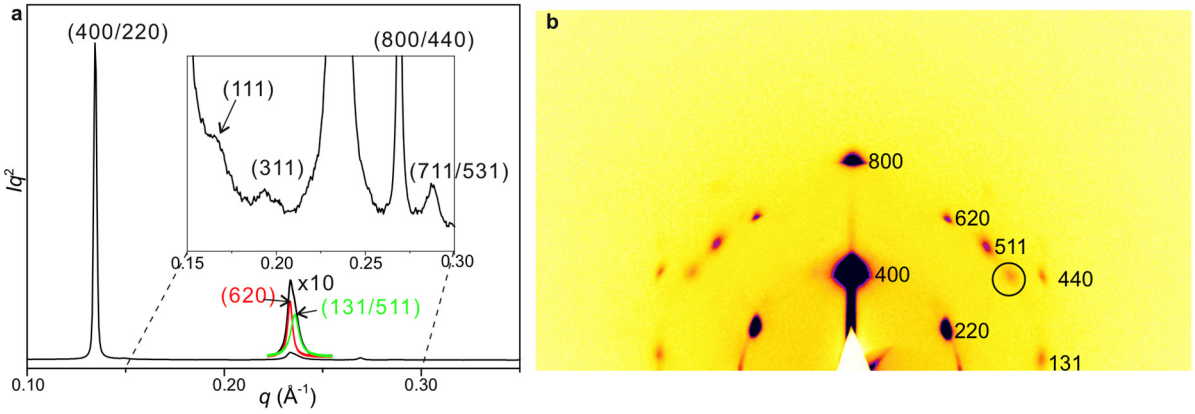

Supplementary Fig. S6 a, Powder SAXS curve and **b**, GISAXS pattern of *Fddd* phase of **IC^3/14** recoded at 60 °C (cooled from 80 °C). The black circled spots are (511) from the other orientation. More details of the other orientation can be seen in Figure S10. As the *d*-spacings of (620) and (511/131) are close with each other, it is shown in one peak in powder SAXS. The separated and fitted peaks are displayed in the figure.

Supplementary Table S3 Indices, experimental, calculated *d*-spacings, intensities, phases and lattice parameters of diffraction peaks of **IC^3/14** recorded by transmission powder SAXS in the *Fddd* phase at 60 °C (cooled from 80 °C). All the intensities are Lorentz and multiplicity corrected.

(*hkl*)	experimental *d*-spacings (Å)	calculated *d*-spacings (Å)	*Intensity*
(400)[a] (220)	46.7	46.7	100.0 93.0
(111)	37.4	37.4	0.3
(311)	32.5	32.5	0.5
(620)	27.0	27.0	1.4
(511)[b] (131)	26.8	26.7 26.7	0.8 0.1
(800) (440)	23.4	23.4 23.3	1.1 1.0
(711)[c] (531)	21.9	21.9	0.3 0.3
a = 186.8 Å, b = 107.8 Å and c = 40.8 Å			

a: As (400) is on the meridian of the GISAXS pattern, its intensity cannot be accurately determined (sensitive to incident beam angle and distribution of domain orientations), consequently it is not possible to determine the (400) and (220) intensity ratio in the same way as described before for (511) and (620) peaks of **IC^3/12**. It is assumed that the ratio of the two is the same as that of two in powder SAXS of **IC^3/12**. Similar treatment is used to calculate the intensities of (800) and (440).

b: The ratio of the intensities of (511) and (131) from the GISAXS pattern can be calculated to be 0.85:0.15.

c: As the intensities of (711) and (531) are too weak to be observed in GISAXS pattern, the contribution of them in powder SAXS is assumed to be the same as in **IC^3/12**.

FCN16

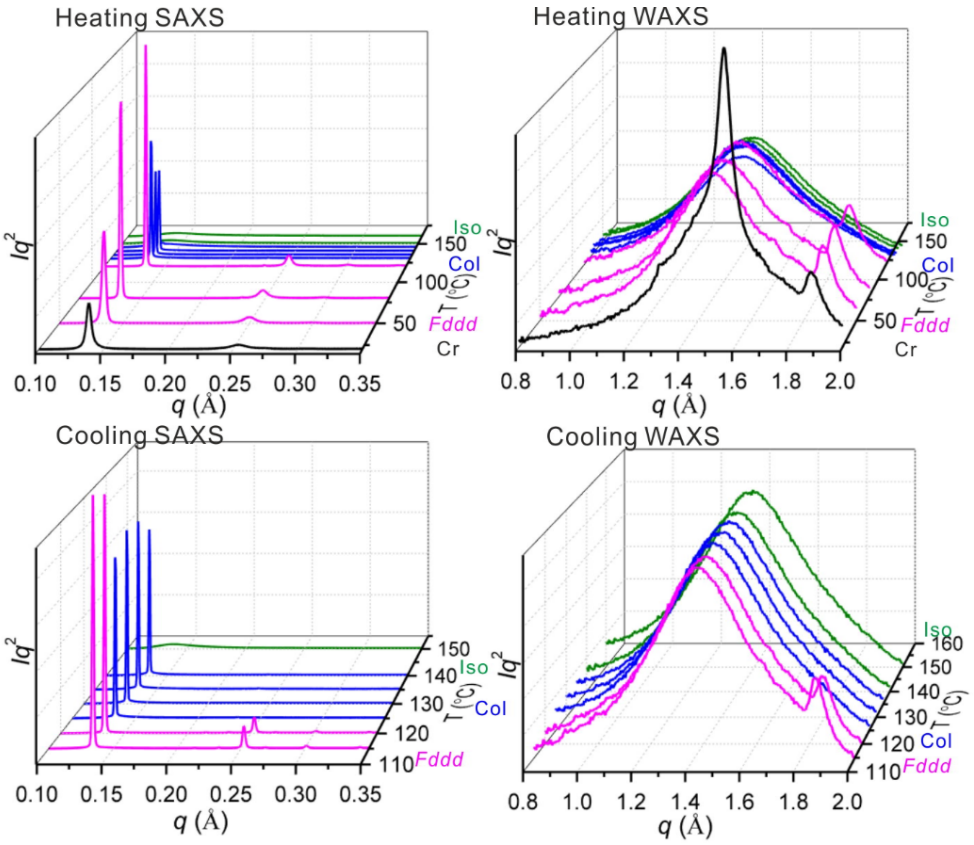

Supplementary Fig. S7 SAXS/WAXS heating and cooling scans of **FCN16**.

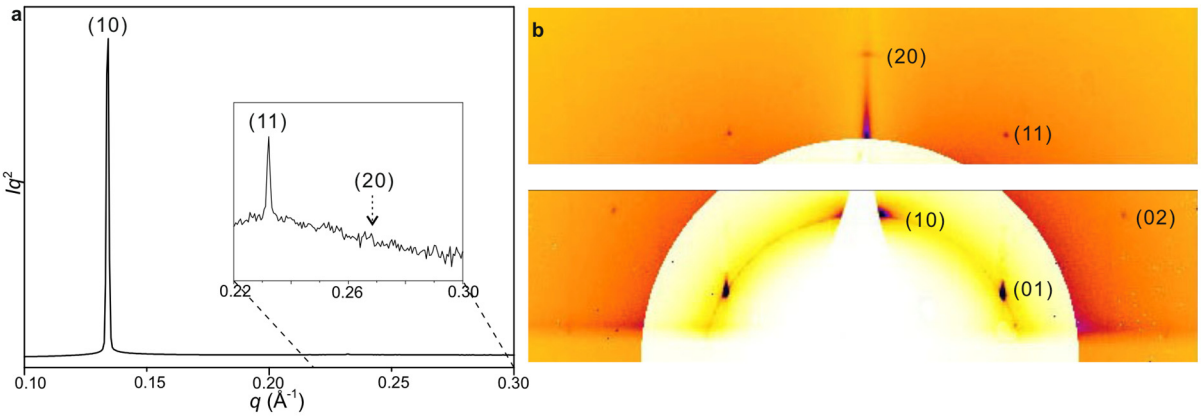

Supplementary Fig. S8 a, Powder SAXS curve and **b**, GISAXS pattern of Col phase of **FCN16** recoded at 130 °C (cooled from 150 °C). In SAXS curve, the intensity of (20) is too weak to be observed, as indicated by the arrow.

Supplementary Table S4 Indices, experimental, calculated *d*-spacings, intensities, phases and lattice parameters of diffraction peaks of **FCN16** recorded by transmission powder SAXS in the Col phase at 130 °C (cooled from 150 °C). All the intensities are Lorentz and multiplicity corrected.

(*hk*)	experimental *d*-spacings (Å)	calculated *d*-spacings (Å)	*Intensity*	*Phase*
(10)	46.9	46.9	100.0	0
(11)	27.1	27.1	0.03	0
(20)	-	23.4	-	-
a = 54.1 Å				

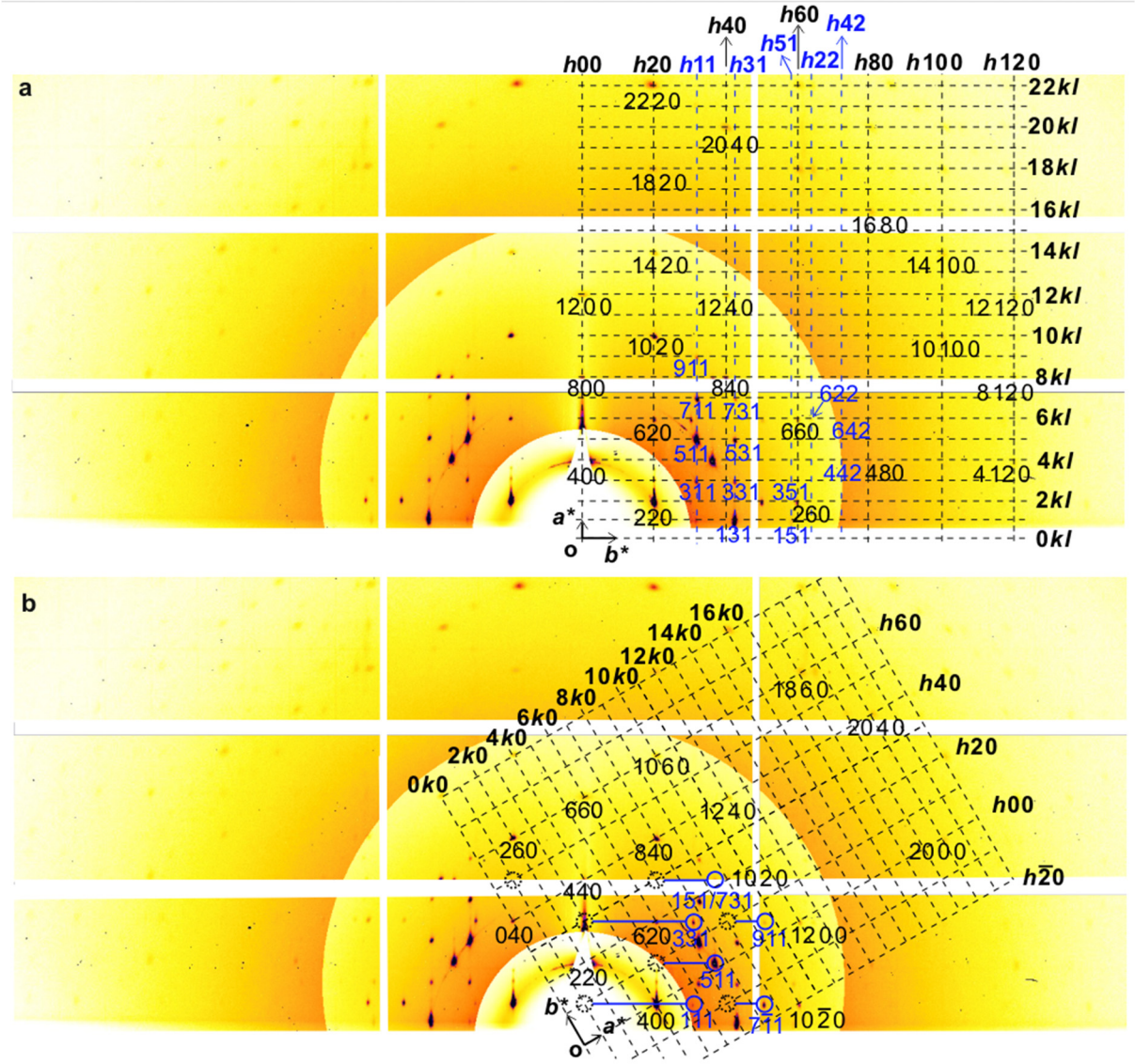

Supplementary Fig. S9 a, **b** The GISAXS pattern of *Fddd* phase of **FCN16** recoded at 120 °C (cooled from 150 °C). In b, some *hkl* spots are circled blue and connected to their *hk*0 base by blue row lines. The position of the projection of reflection (*hkl*) rotating around (110) on the 2D plane is calculated by $\left(\sqrt{\frac{h^2}{a^2}+\frac{l^2}{b^2}+\frac{l^2}{c^2}-\frac{(\frac{h}{a^2}+\frac{k}{b^2})^2}{\frac{1}{a^2}+\frac{1}{b^2}}}, \frac{\frac{h}{a^2}+\frac{k}{b^2}}{\sqrt{\frac{1}{a^2}+\frac{1}{b^2}}}\right)$.

Supplementary Table S5 Indices, experimental, calculated *d*-spacings, intensities, phases and lattice parameters of diffraction peaks of **FCN16** recorded by transmission powder SAXS in the *Fddd* phase at 120 °C (cooled from 160 °C). All the intensities are Lorentz and multiplicity corrected.

(*hkl*)[a]	experimental *d*-spacings (Å)	calculated *d*-spacings (Å)	*Intensity*	*Phase*
(400) (220)	46.7	46.7	100.0 93.0	π π
(111)	32.7	32.7	0.1	-
(311)	29.2	29.3	0.2	-
(620)	27.0	27.0	0.4	-
(511) (131)	24.8	24.8	8.4 1.5	π π
(331)	23.3	23.2	0.2	-
(711) (531)	20.8	20.8	0.6 0.6	π 0
(731) (151)	18.3	18.3	0.2 0.2	- -
a = 186.9 Å, *b* = 107.9 Å and *c* = 34.9 Å				

a: The calculation of the contribution of each reflection (*hkl*) to overlapped peaks in powder diffraction pattern was the same as in **IC^3/12** and **IC^3/14**.

FO16

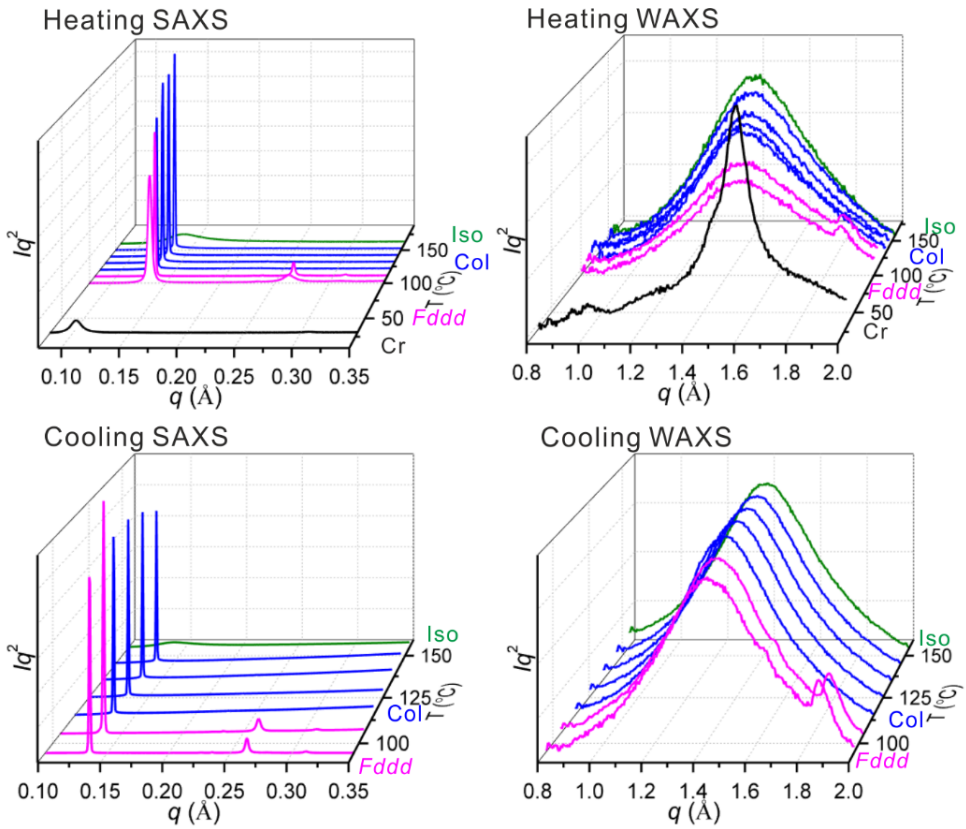

Supplementary Fig. S10 SAXS/WAXS heating and cooling scans of **FO16**.

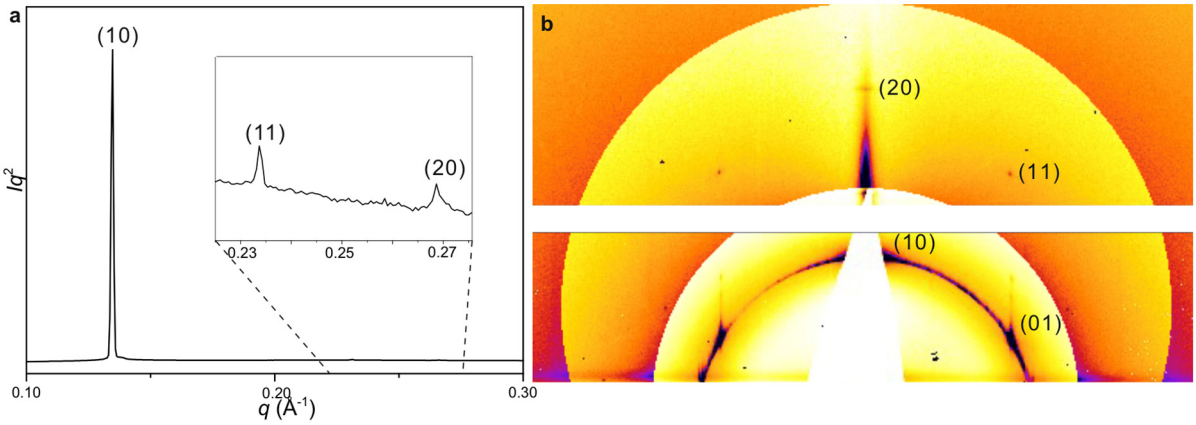

Supplementary Fig. S11 a, Powder SAXS curve and **b**, GISAXS pattern of Col phase of **FO16** recoded at 135 and 130°C, respectively (cooled from 150 °C).

Supplementary Table S6 Indices, experimental, calculated *d*-spacings, intensities, phases and lattice parameters of diffraction peaks of **FO16** recorded by transmission powder SAXS in the Col phase at 135 °C (cooled from 150 °C). All the intensities are Lorentz and multiplicity corrected.

(*hk*)	experimental *d*-spacings (Å)	calculated *d*-spacings (Å)	*Intensity*	*Phase*
(10)	46.7	46.7	100	0
(11)	27.0	27.0	0.2	0
(20)	23.4	23.3	0.1	π
a = 53.9 Å				

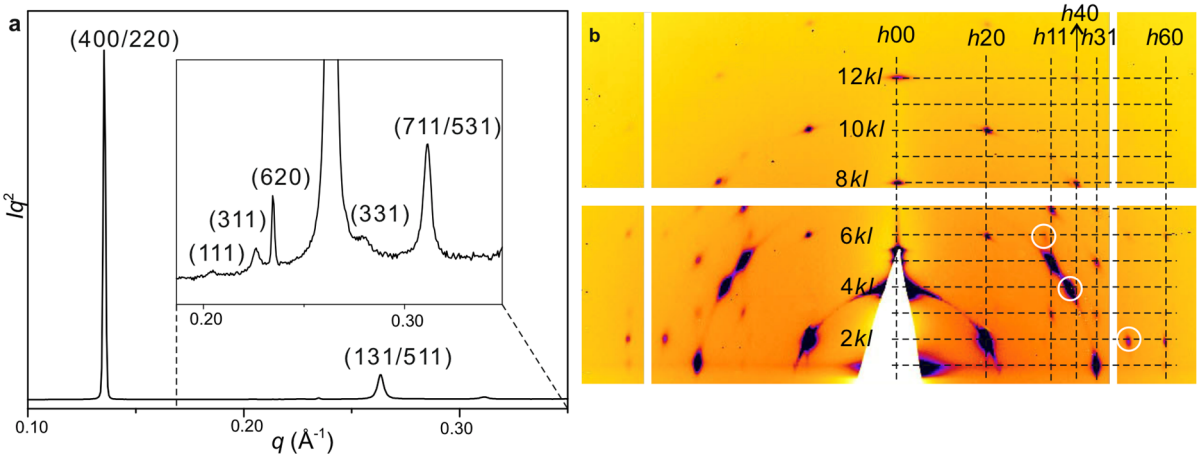

Supplementary Fig. S12 a, Powder SAXS curve and **b**, GISAXS pattern of *Fddd* phase of **FO16** recoded at 105 °C (cooled from 150 °C). The white circled spots are (511), (331) and ($7\bar{1}1$) from the other orientation.

Supplementary Table S7 Indices, experimental, calculated *d*-spacings, intensities, phases and lattice parameters of diffraction peaks of **FO16** recorded by transmission powder SAXS in the *Fddd* phase at 105 °C (cooled from 160 °C). All the intensities are Lorentz and multiplicity corrected.

(*hkl*)[a]	experimental *d*-spacings (Å)	calculated *d*-spacings (Å)	*Intensity*
(400) (220)	46.5	46.5	100.0 93.0
(111)	30.7	30.7	0.3
(311)	27.8	27.8	0.07
(620)	26.7	26.7	0.5
(511) (131)	23.9	23.9	4.0 0.7
(331)	22.4	22.4	0.4
(711) (531)	20.2	20.2	0.1 0.1
a = 186.0 Å, *b* = 107.4 Å and *c* = 32.5 Å			

a: The calculation of the contribution of each reflection (*hkl*) to overlapped peaks in the powder diffraction pattern was the same as in **IC^3/12** and **IC^3/14**.

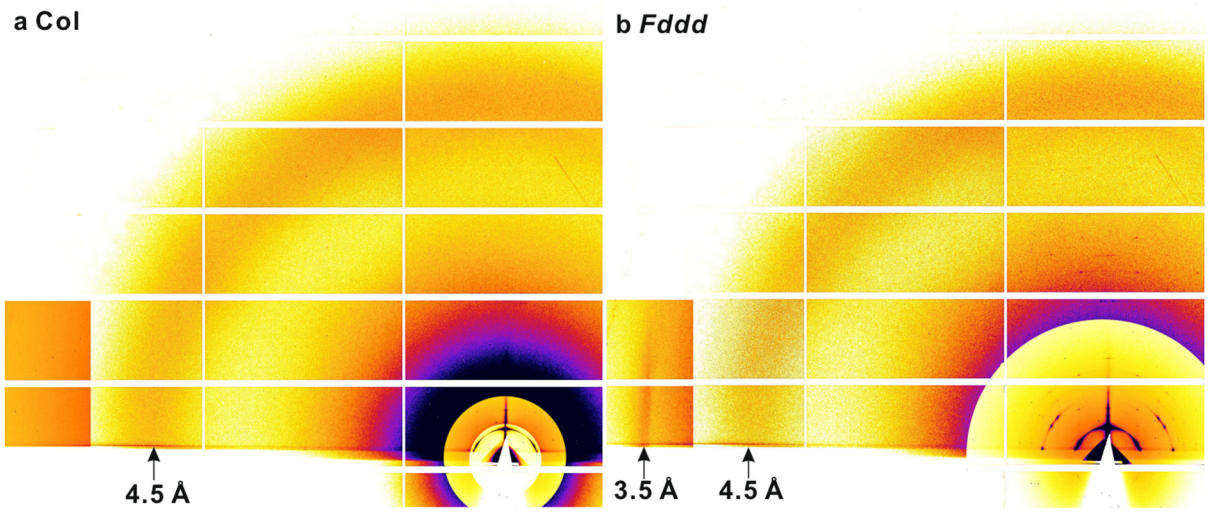

Supplementary Fig. S13 GIWAXS/GISAXS patterns of **a** Col and **b** *Fddd* of **FO16** recorded at 115 °C and 90 °C, respectively.

S4. Reconstruction of electron density maps

Starting with **IC^3/12**, its three strongest peaks (220), (400) and (511) in Table S1 are used to reconstruct the electron density (ED) map of the low-T phase based on *Fddd* symmetry. As *Fddd* is centrosymmetric, there are eight possible phase combinations as the phase of each peak can be only 0 or π. Some of these phase combinations are equivalent by simple shift of origin or full phase inversion. This made the choice of (0π0) as the correct combination very easy, considering that the structure should be closely related to the Col phase of IC^3/n, judging by the negligible or small changes in POM texture, birefringence and transition enthalpy.

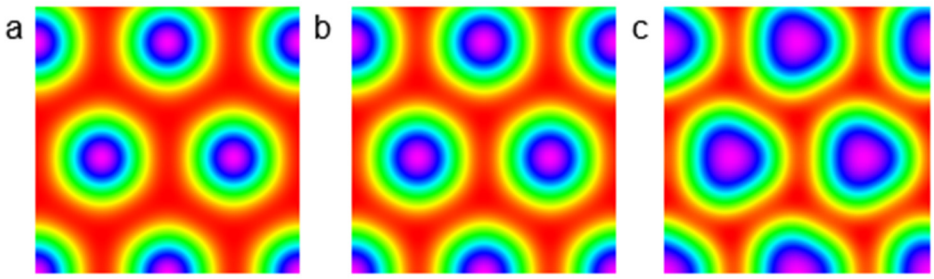

Supplementary Fig. S14 ED maps of Col phases of **a FCN16**, **b FO16** and **c IC^3/12**[1].

S5. Estimate of the number of molecules per column stratum

Supplementary Table S8 Calculation of number of molecules per column stratum of *Fddd* and Col.
n_1 = number of molecules in a unit cell
n_2 = number of molecules per column of length c in *Fddd* phase
n_3 = number of strata in a column of length c in *Fddd* phase
n_4 = number of molecules per column stratum of *Fddd* phase

Name	*Lattice parameters* Å	V_{cell} (Å^3*10^3)[a]	V_{mol} (Å^3*10^3)[b]	A /A per column (Å^2*10^2)[c]	n_1[d]	n_2[e]	n_3[f]	n_4[g]	α[h]
IC^3/10	Col: a = 48.9	9.0 (c = 4.3)	2.99	20.7	3.0	-	-	-	-
IC^3/12	*Fddd:* a = 173.5 b = 106.1 c = 40.8	751.1	3.39	184.1 / 23.0	222.2	27.8	9.1	3.0	13.3
	Col: a = 51.3	10.1 (c = 4.5)		22.8	3.0	-	-	-	-
IC^3/14	*Fddd:* a = 186.8 b = 107.8 c = 40.8	821.6	3.78	201.4 / 25.2	217.4	27.2	9.1	3.0	13.3
	Col: a = 52.8	11.3 (c = 4.7)		24.1	3.0	-	-	-	-
FCN16	*Fddd:* a = 186.9 b = 107.9 c = 34.9	703.7	3.82	201.7 / 25.2	184.3	23.0	10.0	2.3	18.0
	Col: 54.1	11.4 (c = 4.5)		25.3	3	-	-	-	-
FO16	*Fddd:* a = 186.0 b = 107.4 c = 32.5	649.2	3.76	199.8 / 25.0	172.8	21.6	9.3	2.3	19.4
	Col: a = 53.9	11.3 (c = 4.5)		25.2	3.0	-	-	-	-

a: Volume of a unit cell (V_{cell}). *Fddd*: $V_{cell} = a*b*c$; Col: $V_{cell} = a^2 c \sin 60°$ (For Col phase, by analogy with similar compounds, c is estimated to be around 4.5 Å and is adjusted to make n_1 an integer number).
b: Volume of molecule: $V_{mol} = V_{arom} + V_{aliph}$; V_{arom} = volume of aromatic part of the molecule calculated using the crystal volume increments[2]; V_{aliph} = volume of aliphatic part of the molecule assuming a density of about 0.8 g/cm^3 (density of liquid alkanes).
c: Unit cell area A of *Fddd* in ab plane: $A = ab$; unit cell area A of each column: $A = ab/8$; unit cell area of Col: $A = a^2 \sin 60°$.
d: Number of molecules in a unit cell: $n_1 = V_{cell} / V_{mol}$.
e: Number of molecules per column of length c in *Fddd* phase: $n_2 = n_1 / 8$.
f: Number of strata in a column of length c in *Fddd* phase: $n_3 = c$ / 4.5 Å (for **IC^3**; estimated) or 3.5 Å (determined for **FCN16** and **FO16** from the position of the meridional peak in GIWAXS).
g: Number of molecules per column stratum of *Fddd* phase $n_4 = n_2 / n_3$.
h: Twist angles α between strata. For **IC^3/n**, $\alpha = 120°/n_4$; For **FCN16** and **FO16**, $\alpha = 180°/n_4$.

Supplementary Table S9 Lattice parameters ratio comparison.

Compound name[a]	*c*:*b*:*a*
Block copolymers[3]	0.500:1:1.732
IC^3/12	0.385:1:1.635
IC^3/14	0.378:1:1.733
FCN16	0.323:1:1.732
FO16	0.298:1.732

a: The lattice parameter *a* is defined as the largest one.

S6. Additional schematic models with ED maps

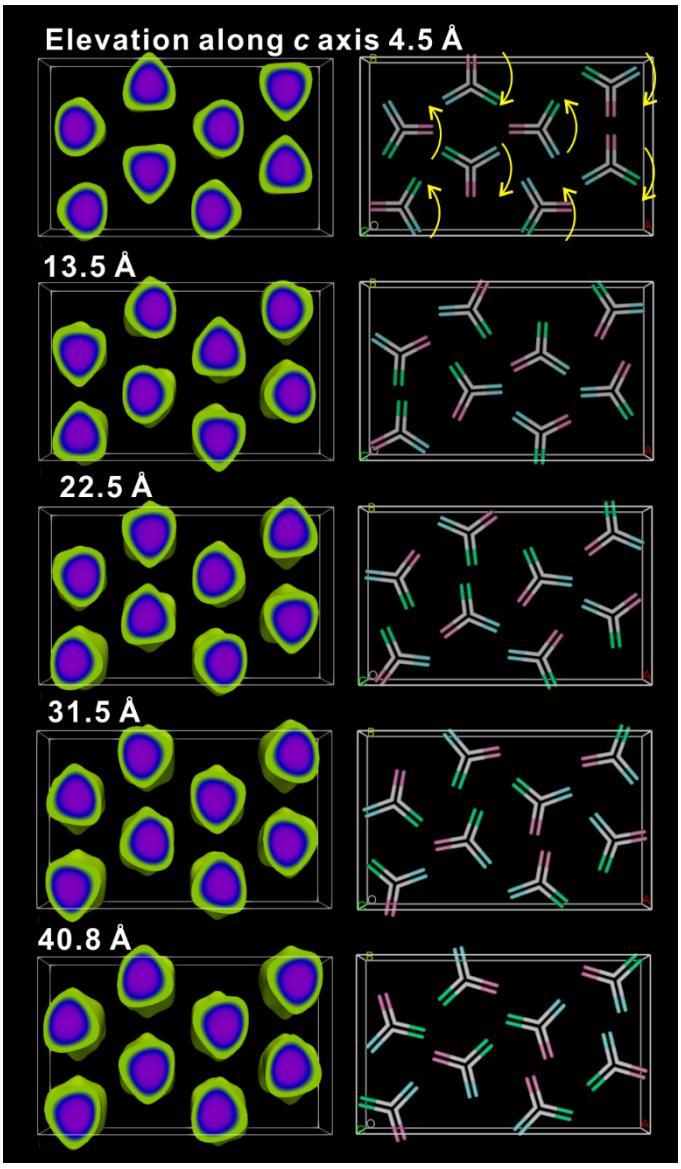

Supplementary Fig. S15 Detailed ED maps (high ED region) and sketched models viewing along *c*-axis with different layers of **IC^3/12** (see also videos 1.1-1.3).

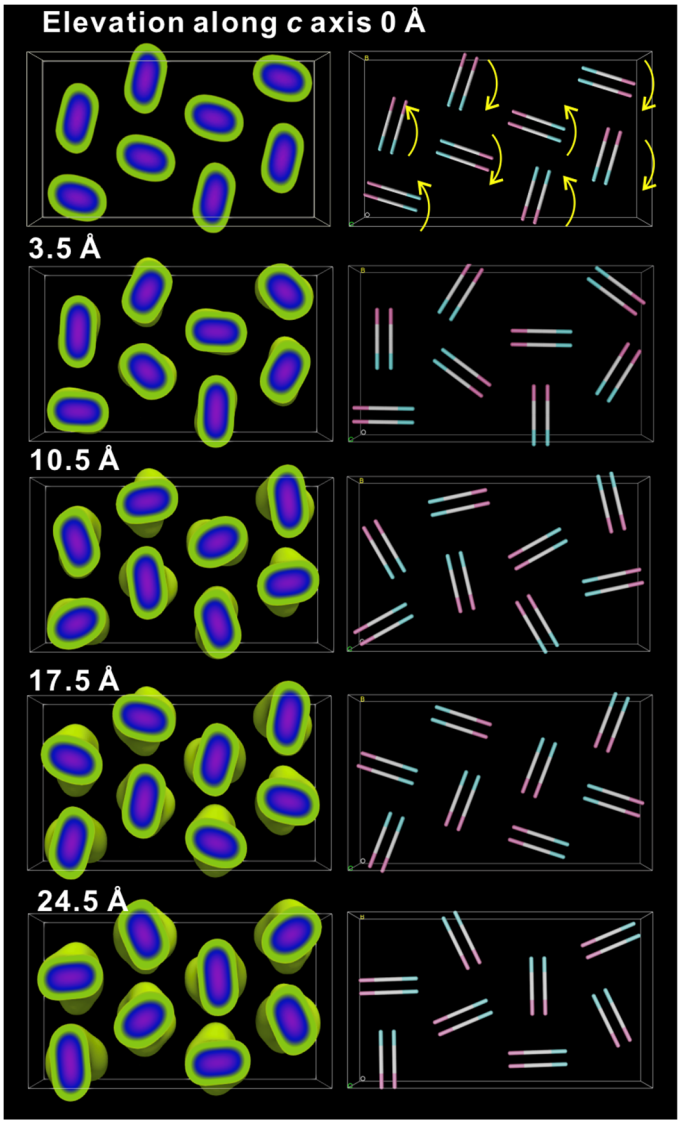

Supplementary Fig. S16 Detailed ED maps (high ED region) and sketched models viewing along *c*-axis with different layers of **FCN16** (see also videos 2.1-2.3).

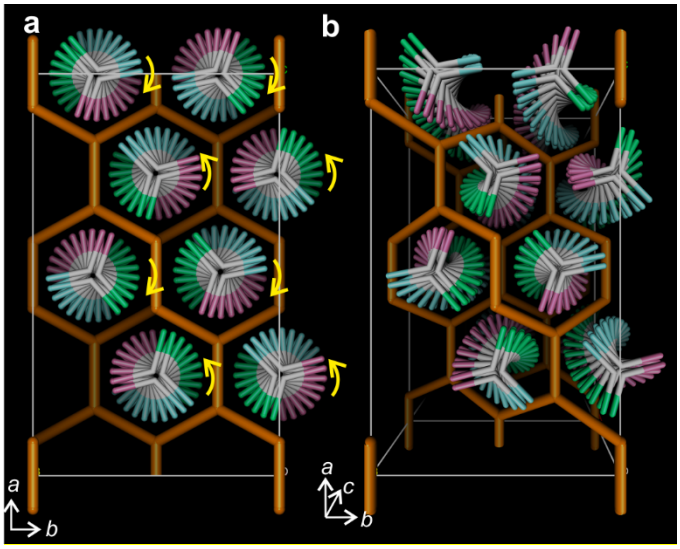

Supplementary Fig. S17 Additional schematic *Fddd* models, comparing the single network model formed by block copolymers with the model of **IC^3/n**.

S7. Additional AFM images

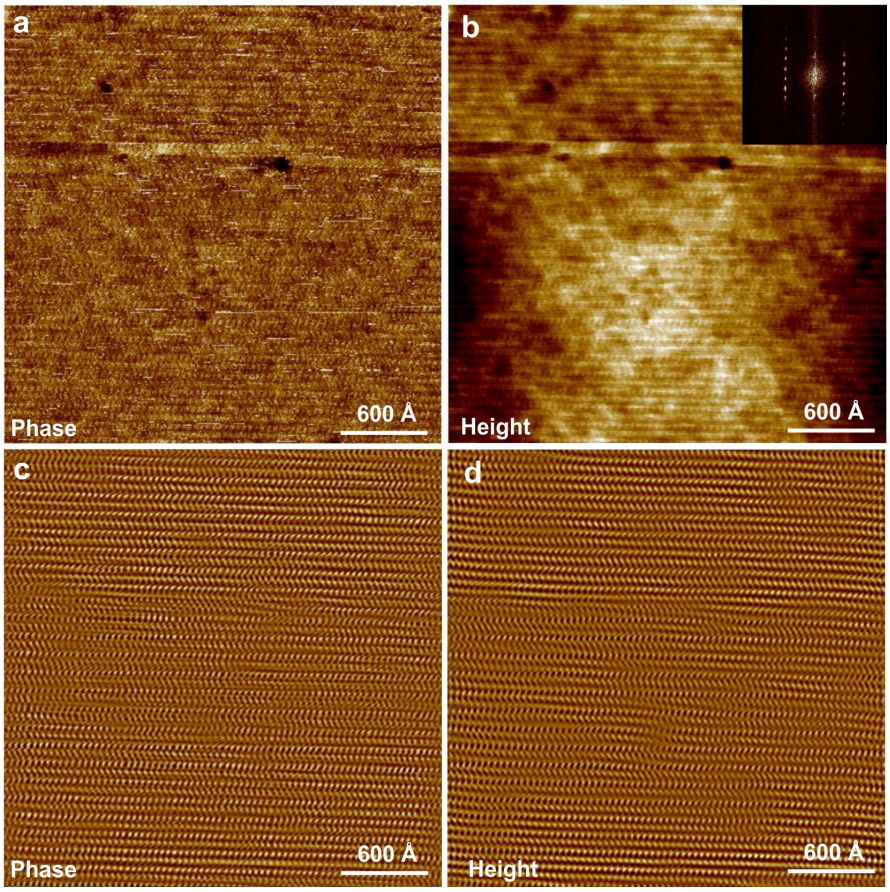

Supplementary Fig. S18 AFM of **FCN16 in the *Fddd phase* at 50°C: a**, **b** original phase and height images; **c**, **d** corresponding Fourier filtered images. Inset in (**b**) shows the Fourier transform of (**b**).

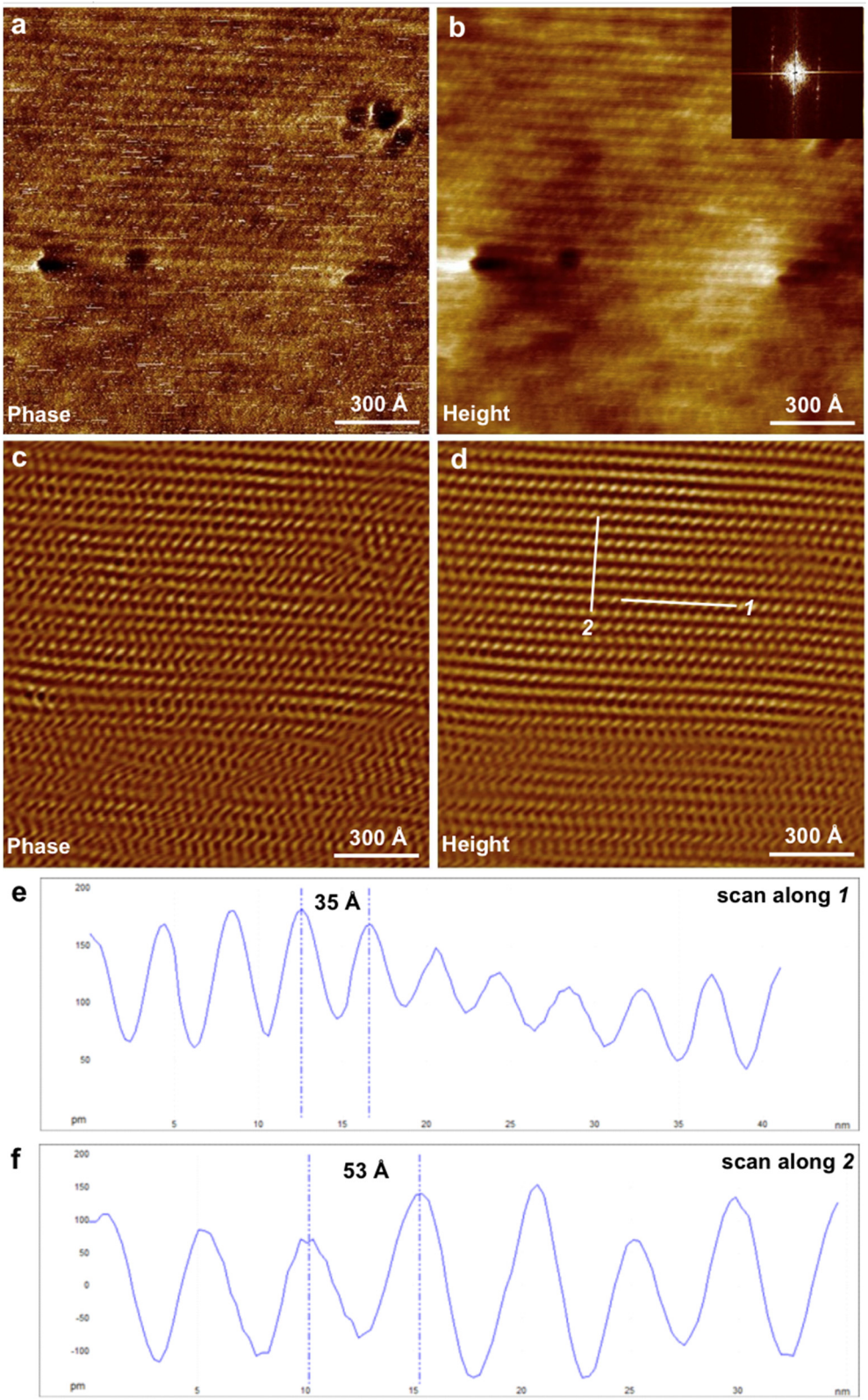

Supplementary Fig. S19 AFM of **FCN16 in the *Fddd phase* at 50°C at higher magnification: a**, **b** original phase and height images; **c**, **d** corresponding Fourier filtered images; **e**, **f** scanned spectra along the two axes of (**d**).

S8. UV-vis and fluorescence emission spectroscopy

Supplementary Table S10 UV-vis and Fluorescence Emission results

Compound	phase	Absorption λ_{max}/nm	Band-gap/eV[a]	Emission λ_{max}/nm[b]	Stokes shift (nm)
FCN16	Col	209, 396, 652	1.52 (130 °C)	-	-
FCN16	*Fddd*	209, 412, 696-714	1.42 (120 °C) 1.35 (30 °C)	-	-
FO16	Col	209, 316, 384, ~500	2.15 (110 °C)	625-633	113-121
FO16	*Fddd*	211, 321, 396, ~520	2.13 (100 °C) 2.10 (40 °C)	642-646	130

a: Band-gap, based on the longest wavelength absorption, is calculated by the Tauc plot method[4]. The band-gap of **FCN16** is smaller than that of **FO16** due to the stronger electron-accepting ability of the fluoren-9-ylidene)malononitrile group.

b: λ_{max} in Emission spectra.

S9. Minimum energy packing of helical columns

We have developed a simple quantitative theory in order to examine the interactions and packings of helical columns, and to explore their possible minimum energy structures. The theory suggests that the *Fddd* structure is indeed the minimum energy structure from packing of helical columns, among the different candidate structures we have explored.

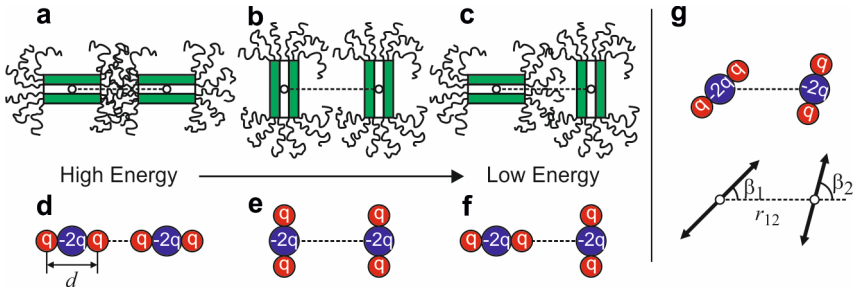

Supplementary Fig. S20 (a-c) Different orientations of two dimers of straight core phasmids in neighbouring columns result in different system energies. (a) Highest energy state due to heavy clashes between aliphatic chain ends of the dimers. (b) Medium energy state due to inefficient packing of space (voids between straight cores of the dimers). (c) Minimum energy state where the space is efficiently packed with little clashes between chain ends. Such energy landscape matches that from the interaction of two linear quadrupoles, with the orientations of the quadrupoles the same as those of the dimers (d-f). (g) The interaction energy between two linear quadrupoles are linked to their distance r_{12} and their orientations as defined by angles β_1 and β_2.

In **FCN16** and **FO16**, the basic unit of the helical column is the dimer. In each stratum of the helical column there are two molecules, with their straight cores parallel to each other and six flexible aliphatic chains at each ends of the dimer core (**Fig. 4d**). As shown in **Fig. S20a-c**, how efficiently the space is filled between two columns very much depends on the orientations of the dimers in two neighbouring columns. The interaction energy between the two dimers is high if they are pointing at each other as

their chain ends would clash. There is less clash between two dimers if they are pointing away from each other (**Fig. S20b**), but the voids between the two dimers means inefficiency in space packing hence it is high energy too. The best packing of space is achieved when one dimer is pointing directly at the other, while the other is pointed way (oriented perpendicular to the other), as in **Fig. S20c**. Interestingly, such dependence of interaction energy between the dimers on their orientations is very much similar to that between two linear quadrupoles, as shown in Figure S1d-f, the energy is highest when the two quadrupoles are pointing at each other, lowest when one of them points at another, while the other points perpendicularly away.

The interaction energy between two quadrupoles, with quadrupole moment $\phi = 3qd^2$ (q is the partial charge at the ends and d is the length of the quadrupole, as shown in **Fig. S20d**), is

$$E_{\phi-\phi} = A\frac{\phi^2}{r_{12}^5}$$

Where r_{12} is the distance between the two quadruples and A is the factor linked to the orientations of the two quadrupoles. In our case the two quadrupoles are in the same plane and their orientations are defined by two angles β_1 and β_2 (**Fig. S20g**)[5].

$$A = 3\cos(2\beta_1 + 2\beta_2) + \frac{9}{16}\cos 2\beta_1 \cos 2\beta_2 + \frac{15}{16}\cos 2\beta_1 + \frac{15}{16}\cos 2\beta_2 + \frac{9}{16}$$

The minimum values of A is found with $\beta_1 = 0$ and $\beta_2 = \pi/2$ (or $\beta_1 = \pi/2$ and $\beta_2 = 0$), with $A_{min} = -3$. The maximum value of A is found with $\beta_1 = \beta_2 = 0$, with $A_{max} = 6$. For random arrangement of β_1 and β_2, the averaged A is $A_{ave} = 9/16$.

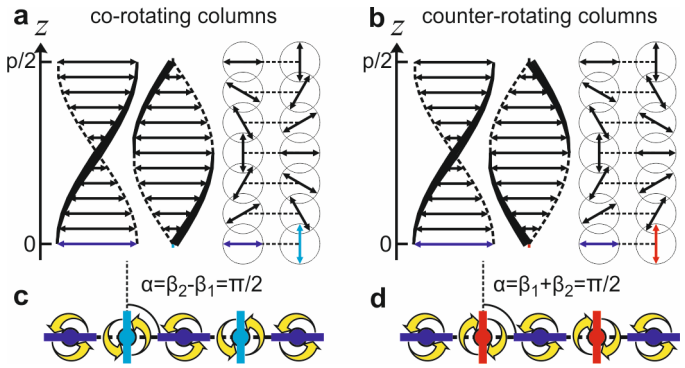

Supplementary Fig. S21 (a, b) Side and projected views of minimum energy neighbouring co-rotating (a) and counter-rotating (b) helical columns. Twisting of dimers along the columnar direction (z-axis) is represented as a series of twisting linear quadrupoles. (c,d) The minimum energy 1D array of helical columns, with nearest neighbours always co-rotating (c) or counter-rotating (d). The rotating direction of each column is shown by yellow arrows, and the orientation of the quadrupole at z=0 is shown by the coloured rod at the centre. The interaction between two neighbouring co-rotating and counter-rotating helices depends on an angle α. For co-rotating helical columns $\alpha = \beta_2 - \beta_1$, and for counter-rotating ones $\alpha = \beta_1 + \beta_2$. Here β_1 and β_2 define the orientations of the two quadrupoles, one from each column, at the same z-level. α is a constant independent of z and defines the relative orientation of the two helical columns.

To calculate the interaction energy of two helical columns, each of which consists of a series of dimers represented by quadrupoles, with the direction of dimer/quadrupoles twisting along its helical axis (**Fig. S21a,b**), we make the assumption that the helix is continuous, and the interaction between the two helical columns is simply the average of quadrupole interactions at different heights, i.e. we ignore the interactions between dimers from the two columns at different heights. This, even though much simplified, is in fact equivalent to considering the average orientation of dimers/quadrupoles that are

interacting with a dimer/quadrupole from another column, and should carry the essence of such interaction between helical columns.

If the two neighbouring columns are co-rotating, i.e. have the same hand, then at different height we always have $\alpha = \beta_2 - \beta_1$ being a constant (**Fig. S21a**). When the height z goes from 0 to $p/2$, where p is the helical pitch of the column, β_1 changes from 0 to π and β_2 changes from α to $\alpha + \pi$. Average at different heights thus gives the interaction energy per pair of dimers between co-rotating columns as

$$U_{co} = \frac{2\phi^2}{pr_{12}^5}\int_0^{p/2} A_{co}(z)dz = \frac{3\phi^2}{32r_{12}^5}(3\cos 2\alpha + 6)$$

If the two neighbouring columns are counter rotating instead, at different height $\alpha = \beta_1 + \beta_2$ is a constant (**Fig. S21b**). When the height z goes from 0 to $p/2$, β_1 changes from 0 to π and β_2 changes from α to $\alpha - \pi$. Average at different heights thus gives

$$U_{counter} = \frac{2\phi^2}{pr_{12}^5}\int_0^{p/2} A_{counter}(z)dz = \frac{3\phi^2}{32r_{12}^5}(35\cos 2\alpha + 6)$$

In both cases the energy minimum is given by $\alpha = \pi/2$, i.e. when at a particular height the dimer from one column is pointing at another column, while the dimer in the other column at the same height is pointing perpendicularly away. It is also obvious from the calculation that neighbouring counter-rotating helices is more favoured energetically comparing to co-rotating ones. Such behaviour is like that of two intermeshing cogwheels, where they rotate in opposite directions so the teeth of each cogwheel always avoid direct clash with those of another.

The minimum energy configuration of our helical columns can be readily derived in 1D, as all neighbouring columns can be counter rotating and with α angle being $\pi/2$, as shown in **Fig. S21d**. If all the columns have the same handedness hence co-rotating, the 1D minimum energy configuration is shown in **Fig. S21c**, again with all α angles being $\pi/2$. Expressing the energy in the unit of $\frac{3\phi^2}{32r_{12}^5}$, the minimum energy per dimer in a 1D counter-rotating array is -29, that of the co-rotating array is 3, and for a random 1D array (without any z-correlation between columns) the energy per dimer is 6.

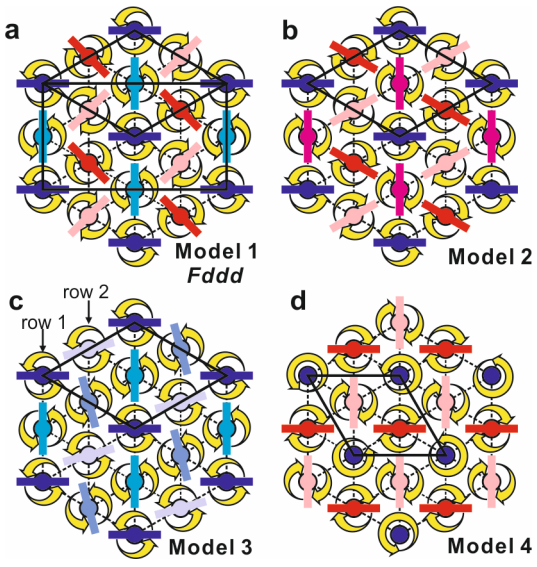

Supplementary Fig. S22 (a) Calculated minimum energy configuration on a 2D hexagonal lattice, with two left- and two right-handed columns in a 2x2 hexagonal unit cell. The result is equivalent to the *Fddd* structure we have observed experimentally. (b) Calculated minimum energy configuration on a 2D hexagonal lattice, with three left- and one right-handed columns in a 2x2 hexagonal unit cell. (c) Calculated minimum energy configuration on a 2D hexagonal lattice, with four right-handed columns in a 2x2 hexagonal unit cell. It turns out that vertical shifting of the second row of columns, in relation to the first row, does not change the system energy. (d) Calculated minimum energy configuration on a

2D hexagonal lattice, with two left- and one right-handed columns in a $\sqrt{3} \times \sqrt{3}$ hexagonal unit cell. The orientation of the right-handed (red) columns can be random without affecting the system energy.

However, the condition to keep all neighbouring columns counter-rotating cannot be satisfied on a 2D hexagonal lattice, as around each triangle in the lattice there are three columns neighbouring to each other, and at least two of them must have the same hand. The obvious choice to minimize the system energy is to keep as many counter-rotating neighbours for each column as possible. As shown in **Fig. S22a**, a 2x2 periodic supercell is assumed, as both counter- and co-rotating minimum energy 1D columns have a repetition every two columns (with α angle being $\pi/2$). We have two left-and two right-handed helical columns in the unit cell, and each column has four counter rotating and two co-rotating neighbouring columns (a ratio of 2:1). It is also not possible to make all rows of co-rotating and counter-rotating columns to have α angles of $\pi/2$. Energy minimization shows that all co-rotating columns have αangles of $\pi/2$, and all counter-rotating columns have an α angle of $5\alpha/12$ (**Fig. S22a**), with an average energy per dimer of about –45.6 (in unit of $\frac{3\phi^2}{32r_{12}^5}$, **Table S11**). The minimum energy configuration fits very well with our experimental observations (**Fig. 4b** in the main text).

While the model shown in **Fig. S22a** seems reasonable, we have also explored other possible configurations on a 2D lattice and these are shown in **Fig. S22b-d**. In the configuration in **Fig. S22b**, we have again a 2x2 superlattice, but with three left-handed and one right-handed columns. While around a right-handed column, all its six neighbouring columns are counter-rotating, for the left-handed columns, four of its neighbouring columns are co-rotating and the other two are counter-rotating. Overall the ratio between counter-rotating neighbours to co-rotating ones is 1:1. While the α angles between counter-rotating columns are $\pi/2$, the α angles between co-rotating columns are $\pi/3$. Due to the reduced number of neighbouring counter-rotating columns, it is no surprise that this structure turns out to have a higher energy than our *Fddd* structure (-36.75 vs -46.5 per dimer in unit of $\frac{3\phi^2}{32r_{12}^5}$, **Table S11**).

When all columns have the same handedness, as shown in **Fig. S22c**, the energy is found to be much higher (15 in unit of $\frac{3\phi^2}{32r_{12}^5}$). There are also many equivalent minimum energy configurations. While row 1 and row 2, as shown in Figure S3e, have α angles of $\pi/2$, the system energy will not be affected by a change in the relative angles (or equivalent shift of the rows in the z-direction) between the two rows.

The other configuration we have studied is shown in **Fig. S22d**, a three-column super-lattice structure similar to that proposed for the so-called "ordered columnar hexagonal" phase found in temperatures below the normal discotic columnar hexagonal phase in Hexa-hexylthiotriphenylene (HHTT)[6]. It has three columns in its unit cell, two left-handed and one-right handed. In its calculated minimum energy configuration, all neighbouring co-rotating columns have α angle of $\pi/2$. The system energy, however, does not depend on the orientation of the right-handed columns at all. The calculated energy turns out to be exactly the same as that of the previous model but much worse than the first two, where rows of counter-rotating columns have been better preserved.

In summary, our theoretical calculations strongly indicate that the *Fddd* structure we have observed is the direct result of optimizing the packing efficiency, and therefore the best structural candidate, of helical columns.

Supplementary Table S11 Calculated minimum interaction energies for different regular configurations of helical columns on a hexagonal lattice, given as average energy per dimer. For comparison, a columnar hexagonal phase of helical columns without any correlation in the *z*-direction between columns has an average energy per column of 18 (in unit of $\frac{3\phi^2}{32r_{12}^5}$).

Model Number	1 (*Fddd*)	2	3	4
Energy per dimer (in $\frac{3\phi^2}{32r_{12}^5}$)	$15-35\sqrt{3}$ (~–45.6)	-36.75	15	15

S10. Synthesis and analytical data

S10.1. General remarks

Reactions requiring an inert gas atmosphere were conducted under nitrogen and the glassware was oven-dried (105 °C). Tetrahydrofuran (THF) was distilled from sodium prior to use. Commercially available chemicals were used as received. ^{1}H-NMR and ^{13}C-NMR spectra were recorded on a Bruker-DRX-300 spectrometer and a Bruker-DRX-400 spectrometer. Elemental analysis was performed using an Elementar VARIO EL elemental analyzer. Thin-layer chromatography was performed on aluminum plates precoated with 5735 silica gel 60 PF254 (Merck). Column chromatography was performed on Merck silica gel 60 (230-400 mesh).

The synthesis of bent phasmid mesogens **IC^3/10**, **IC^3/12** and **IC^3/14** have been reported previously in our publication[1]. The compounds **FO16** and **FCN16** were synthesized using Suzuki coupling reactions as key step as shown in Scheme 1. Firstly, 2,7-dibromo-9H-fluorenone **3** [7] was obtained by the bromination and oxidation of fluorene **1**. Then 2,7-bis(4,4,5,5-tetramethyl-1,3,2-dioxaborolanyl)-9-fluorenone **4** [8] was obtained by the $PdCl_2$(dppf)-catalyzed reaction of the compound **3** with bis(pinacolato)diboron. 2-(4-((3,4,5-Tris(hexadecyloxy)benzyl)oxy)phenyl)thiophene **5** was synthesized according to our previously reported procedures [9]. **5** was brominated with N-bromosuccinimide (NBS) and the obtained 2-bromo-5-(4((3,4,5-tris(hexadecyloxy)benzyl)oxy)phenyl)thiophene **6** was coupled with compound **4** to afford compound **FO16**. Finally, a Knoevenagel condensation between malononitrile and **FO16** led to the target product **FCN16**.

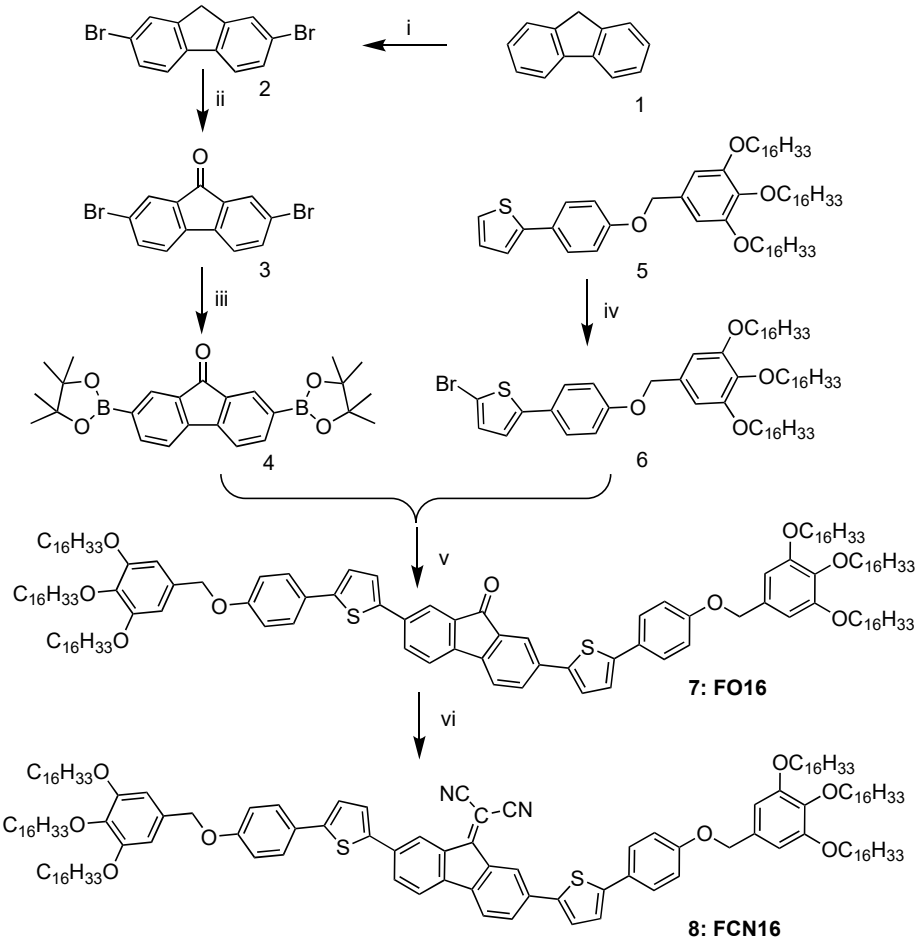

Supplementary Scheme S1. Synthesis of compound **FO16** and **FCN16**, Reagents and conditions: *i*) Br_2, $FeCl_3$, $CHCl_3$, 0 °C; *ii*) CrO_3, CH_3COOH, RT; *iii*) bis(pinacolato)diboron, $PdCl_2$(dppf), KOAc, 1,4-dioxane, 100 °C; *iv*) NBS, THF, 0 °C; *v*) $Pd(PPh_3)_4$, K_2CO_3, THF, H_2O, N_2, 78 °C; *vi*) $CH_2(CN)_2$, pyridine.

S10.2 General procedures for the synthesis of FCN16.

Compound **2**:

Fluorene **1** (500 mg, 3.00 mmol) was dissolved in chloroform (5 mL) and $FeCl_3$ (7.5 mg, 0.046 mmol) was added. The solution was cooled in a water/ice bath to 0 °C. Bromine (0.33 mL, 6.34 mmol) was added dropwise to the stirred mixture. After complete addition the mixture was stirred for an additional three hours. Saturated $Na_2S_2O_3$ solution (20 mL) was slowly added and stirring was continued for 30 minutes. Chloroform (50 mL) was added, the organic phases were separated and the aqueous layer was extracted with chloroform (3 × 50 mL). The combined organic layers were dried over anhydrous Na_2SO_4, filtered and the solvent was evaporated in vacuo. The crude product was purified by a silicagel column chromatography (Petroleum ether) to produce compound **2** as white solid. Yield: 961.8 mg (98.7%). ^{1}H-NMR (300 MHz, $CDCl_3$), δ (ppm): 7.64-7.62 (d, J = 7.2 Hz, 2H, Ar**H**), 7.58-7.52 (t, J = 9.0 Hz, 2H, Ar**H**), 7.49-7.46 (d, J = 8.1 Hz, 2H, Ar**H**), 3.84-3.78 (d, J = 15.6 Hz, 2H, fluorene-9**H**). Elemental analysis calcd (%) for $C_{13}H_8Br_2$ (324.02): C, 48.19; H, 2.49; found: C, 48.37; H, 2.66.

Compound **3**:

A mixture of 2,7-dibromofluorene (896 mg, 2.7 mmol) and CrO_3 (6.00 g, 60.0 mmol) suspended in 25 mL acetic acid, and stirred at room temperature for 12 h. The resulting yellow precipitate was collected by suction filtration, washed with water thoroughly, and dried under vacuum to provide the product as

yellow solid. The crude product was purified by a silicagel column chromatography (Petroleum ether) to produce compound **3** as white solid. Yield: 355 mg (37.9%). ^{1}H-NMR (400 MHz, $CDCl_3$), δ (ppm): 7.78 (s, 2H, Ar**H**), 7.64-7.62 (d, J = 8.0 Hz, 2H, Ar**H**), 7.40-7.39 (d, J = 7.6 Hz, 2H, Ar**H**). Elemental analysis calcd (%) for $C_{13}H_6Br_2O$ (338.00): C, 46.20; H, 1.79; found: C, 46.45; H, 1.91.

Compound **4**:

To a previously degassed 1,4-dioxane (25 mL) solution of 2,7-dibromo-9-fluorenone (300 mg, 0.89 mmol) were added bis(pinacolato)diboron (580 mg, 2.28 mmol), $PdCl_2$(dppf) (40 mg), and KOAc (420 mg, 4.28 mmol), and the mixture was stirred at 100 °C overnight. After the solution was cooled, the dioxane was removed under vacuum, and then CH_2Cl_2 and water were added. The resulting mixture was extracted with dichloromethane (100 mL) twice, and the organic layer was washed with water and brine and then dried over $MgSO_4$. The organic solvent was concentrated in vacuo to yield a dark-black solid. The pure Compound **4** was isolated by silica gel column chromatography (using as eluents 1:15 ethyl acetate/ petroleum ether) as yellow solid. Yield: 200 mg (52.2%). ^{1}H-NMR (400 MHz, $CDCl_3$), δ (ppm): 8.13 (s, 2H, Ar**H**), 7.96-7.94 (d, J = 7.4 Hz, 2H, Ar**H**), 7.57-7.55 (d, J = 7.4 Hz, 2H, Ar**H**), 1.35 (s, 24H, 8C$\mathbf{H}_3$). Elemental analysis calcd (%) for $C_{25}H_{30}B_2O_5$ (432.13): C, 69.49; H, 7.00; found: C, 69.71; H, 7.19.

Compound **5**:

Compound **5** was synthesized according to literature procedures in ref 9.

Compound **6**:

NBS powder (90 mg, 0.51 mmol) was added stepwise to a stirred solution of compound **5** (500 mg, 0.51 mmol) dissolved in dry THF (20 mL) at 0 °C in dark. The mixture was stirred overnight, quenched with water and then was extracted with dichloromethane (3 × 30 mL). The combined organic phase was dried by anhydrous Na_2SO_4.The solvent was evaporated under reduced pressure and the reaction mixture was purified by column chromatography on silica gel using petroleum ether: ethyl acetate (150: 1) as the eluent to afford compound **6** as a white solid. Yield: 320 mg (59.3%). ^{1}H-NMR (300MHz, $CDCl_3$), δ (ppm): 7.45-7.42 (d, J = 8.8 Hz, 2H, Ph**H**), 7.00-6.93 (m, 4H, 2Ph**H**, 2Thiophene**H**), 6.62 (s, 2H, Ph**H**), 4.97 (s, 2H, OC$\mathbf{H}_2$), 4.00-3.93 (q, J = 6.9 Hz, 6H, 3OC$\mathbf{H}_2$), 1.84-1.70 (m, 6H, 3OCH_2C$\mathbf{H}_2$), 1.47 (m, 6H, 3OCH_2CH_2C$\mathbf{H}_2$), 1.26 (m, 72H, 36C$\mathbf{H}_2$), 0.91-0.86 (t, J = 6.6 Hz, 9H, 3C$\mathbf{H}_3$). Elemental analysis calcd (%) for $C_{65}H_{109}BrO_4S$ (1066.55): C, 73.20; H, 10.30; found: C, 73.37; H, 10.52.

Compound **FO16**:

A mixture of Compound **4** (22 mg, 0.05 mmol), Compound **6** (160 mg, 0.15 mmol), K_2CO_3 (83 mg, 0.60 mmol), $Pd(PPh_3)_4$ (5 mg), THF (8 mL) and H_2O (8 mL) was refluxed at 78 °C for 36 h under an argon atmosphere. After the reaction was complete (TLC), the mixture was cooled to RT, and then the reaction mixture was extracted with dichloromethane (3 × 50 mL). The combined organic layer was dried with anhydrous Na_2SO_4, and the solvent was evaporated in *vacuo*. The residue was purified by a silicagel column chromatography (petroleum ether/ dichloromethane = 1 : 1) to produce compound **FO16** as red solid. Yield: 75 mg (68.5%). ^{1}H-NMR (300MHz, $CDCl_3$), δ (ppm): 7.93 (s, 2H, Ph**H**), 7.75-7.72 (m, 2H, Ph**H**), 7.58-7.55 (d, J = 8.7 Hz, 4H, Ph**H**), 7.54-7.51 (d, J = 7.9 Hz, 2H, Ph**H**), 7.36-7.34 (d, J = 3.8 Hz, 2H, Thiophene**H**), 7.21-7.20 (d, J = 3.7 Hz, 2H, Thiophene**H**), 7.02-7.00 (d, J = 8.8 Hz, 4H, Ph**H**), 6.63 (s, 4H, Ph**H**), 4.99 (s, 4H, 2OC$\mathbf{H}_2$), 4.01-3.93 (m, 12H, 6OC$\mathbf{H}_2$), 1.84-1.70 (m, 12H, 6OCH_2C$\mathbf{H}_2$), 1.47 (m, 12H, 6OCH_2CH_2C$\mathbf{H}_2$), 1.25 (m, 144H, 72C$\mathbf{H}_2$), 0.90-0.85 (t, J = 6.6 Hz, 18H, 6C$\mathbf{H}_3$). ^{13}C-NMR (100MHz, $CDCl_3$): δ = 193.44, 158.85, 153.52, 144.44, 142.74, 141.36, 138.30, 135.48, 135.29, 131.79, 131.30, 127.30, 127.09, 124.77, 123.30, 121.21, 120.87, 115.51, 106.37, 73.60,

70.71, 69.37, 32.09, 30.52-29.52 (multi carbons in alkyl chain), 26.31, 26.28, 22.84, 14.25. Elemental analysis calcd (%) for $C_{143}H_{224}O_9S_2$ (2151.48): C, 79.83; H, 10.49; found: C, 79.41; H, 10.18.

Compound **FCN16**:

Malononitrile (9.2 mg, 0.14 mmol) and compound **FO16** (30 mg, 0.014 mmol) were dissolved in dry pyridine (10 mL) and the solution was stirred at 20 °C for 1 h to obtain a brown suspension. Pyridine (10 mL) was added and the mixture was stirred for an additional 5 h, followed by heating to 80 °C for 1 h. Ethanol (20 mL) was added to the solution and the mixture was cooled to 20 °C. A green solid of **FCN16** was obtained after suction filtration and washed by acetonitrile. Yield: 18 mg (58.7%). ^{1}H-NMR (300MHz, $CDCl_3$), δ (ppm): 8.53 (s, 2H, Ph**H**), 7.67-7.64 (m, 2H, Ph**H**), 7.53-7.50 (d, J = 8.7 Hz, 4H, Ph**H**), 7.49-7.46 (d, J = 8.0 Hz, 2H, Ph**H**), 7.28-7.27 (d, J = 3.8 Hz, 2H, Thiophene**H**), 7.13-7.12 (d, J = 3.8 Hz, 2H, Thiophene**H**), 6.98-6.95 (d, J = 8.8 Hz, 4H, Ph**H**), 6.62 (s, 4H, Ph**H**), 4.95 (s, 4H, 2OC**H**$_2$), 4.00-3.93 (d, J = 7.0 Hz, 12H, 6OC**H**$_2$), 1.84-1.70 (m, 12H, 6OCH$_2$C**H**$_2$), 1.47 (m, 12H, 6OCH$_2$CH$_2$C**H**$_2$), 1.26 (m, 144H, 72C**H**$_2$), 0.90-0.86 (t, J = 6.5 Hz, 18H, 6C**H**$_3$). ^{13}C-NMR (100MHz, $CDCl_3$): δ = 158.77, 153.37, 140.53, 140.41, 138.14, 135.41, 135.11, 131.62, 130.98, 127.00, 125.00, 123.44, 123.23, 120.99, 115.33, 106.22, 73.46, 70.55, 69.22, 31.93, 30.37-29.37 (multi carbons in alkyl chain), 26.13, 22.69, 14.10. Elemental analysis calcd (%) for $C_{146}H_{224}N_2O_8S_2$ (2199.52): C, 79.73; H, 10.27; found: C, 79.55; H, 10.06.

S10.3 ^{1}H and ^{13}C NMR spectra for representative compounds

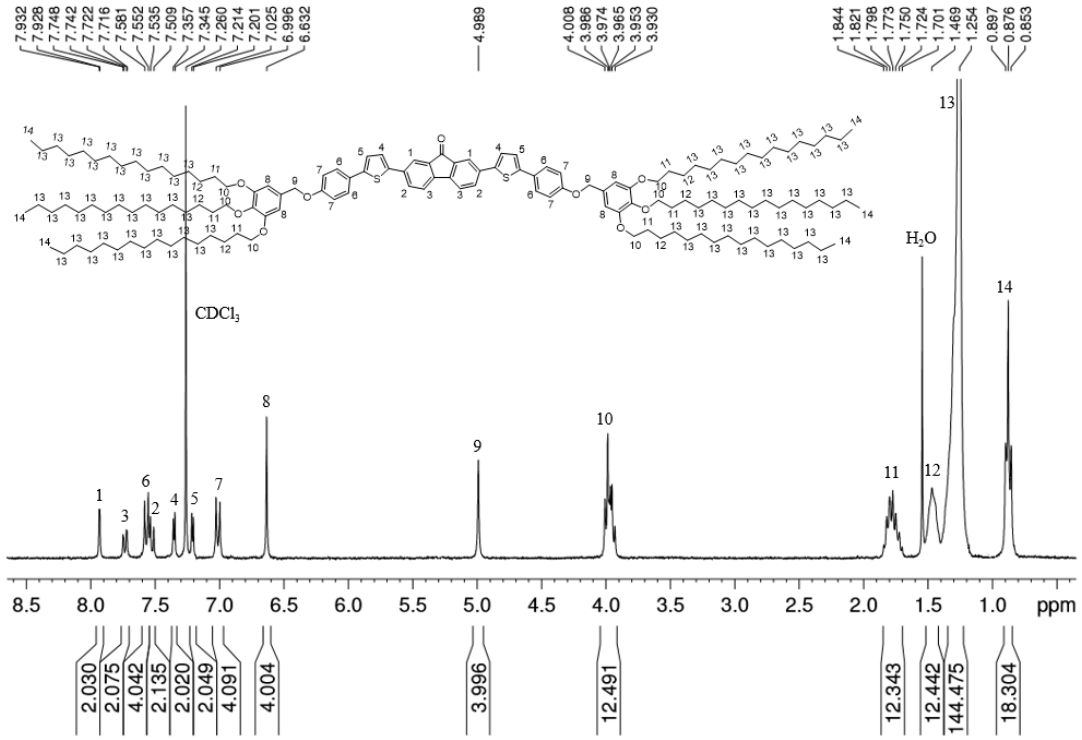

Supplementary Fig. S23 ^{1}H NMR ($CDCl_3$, 400 MHz, ppm) spectra of compound **FO16.**

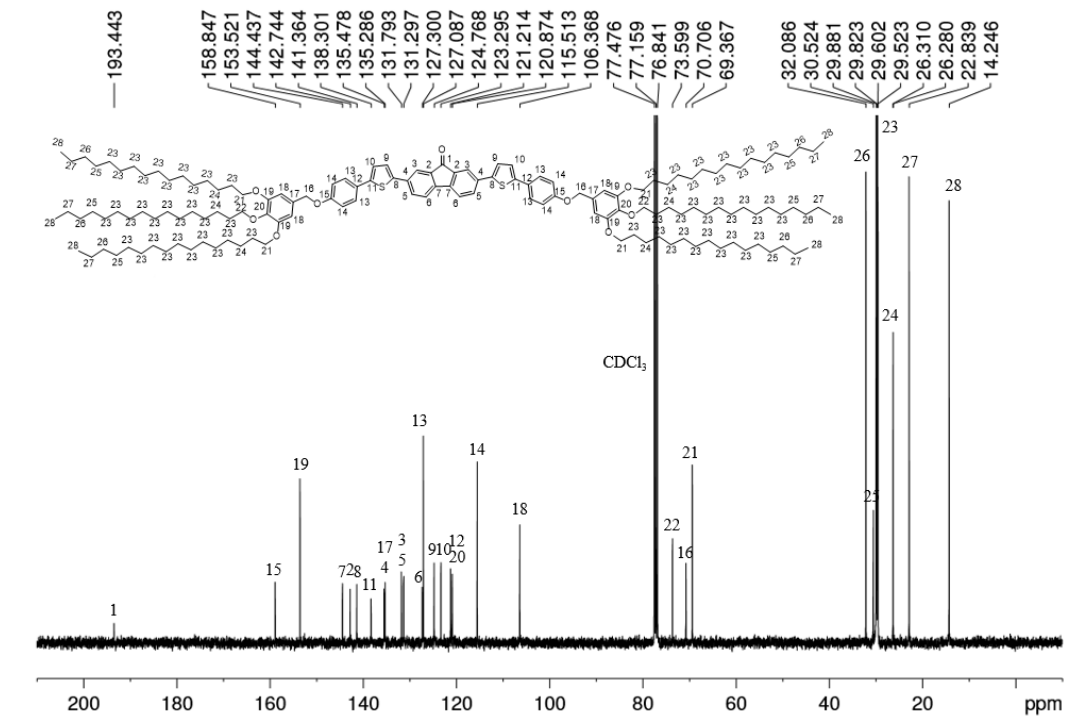

Supplementary Fig. S24 ^{13}C NMR ($CDCl_3$, 100 MHz, ppm) spectra of compound **FO16.**

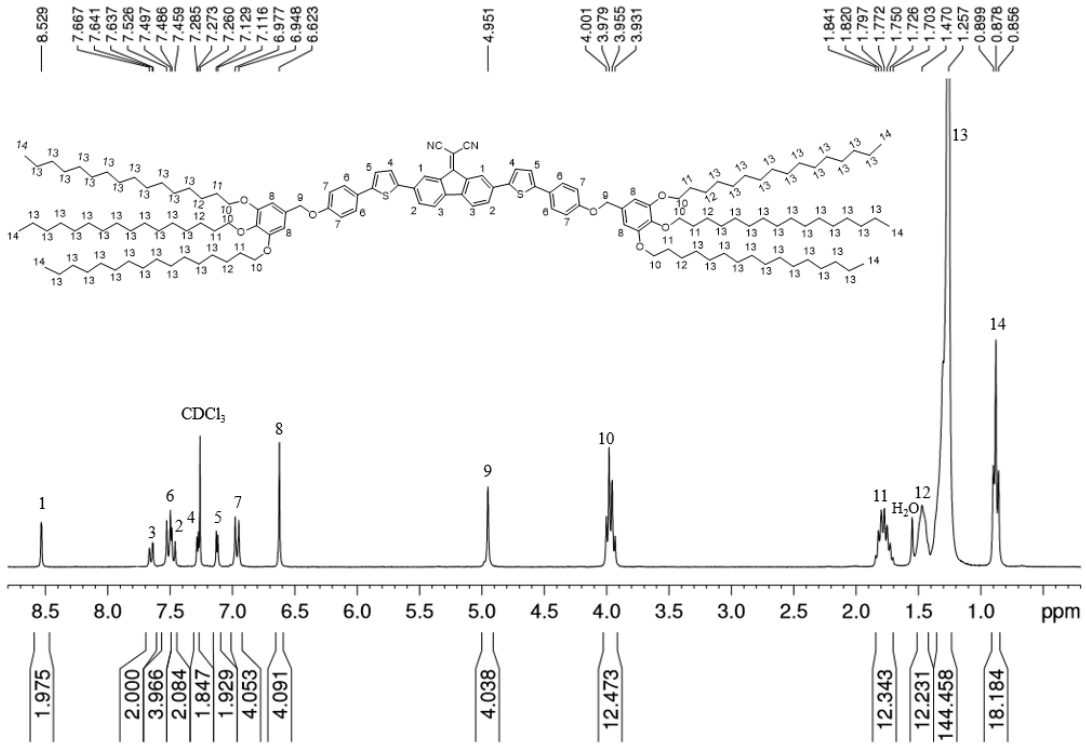

Supplementary Fig. S25 ^{1}H NMR ($CDCl_3$, 400 MHz, ppm) spectra of compound **FCN16.**

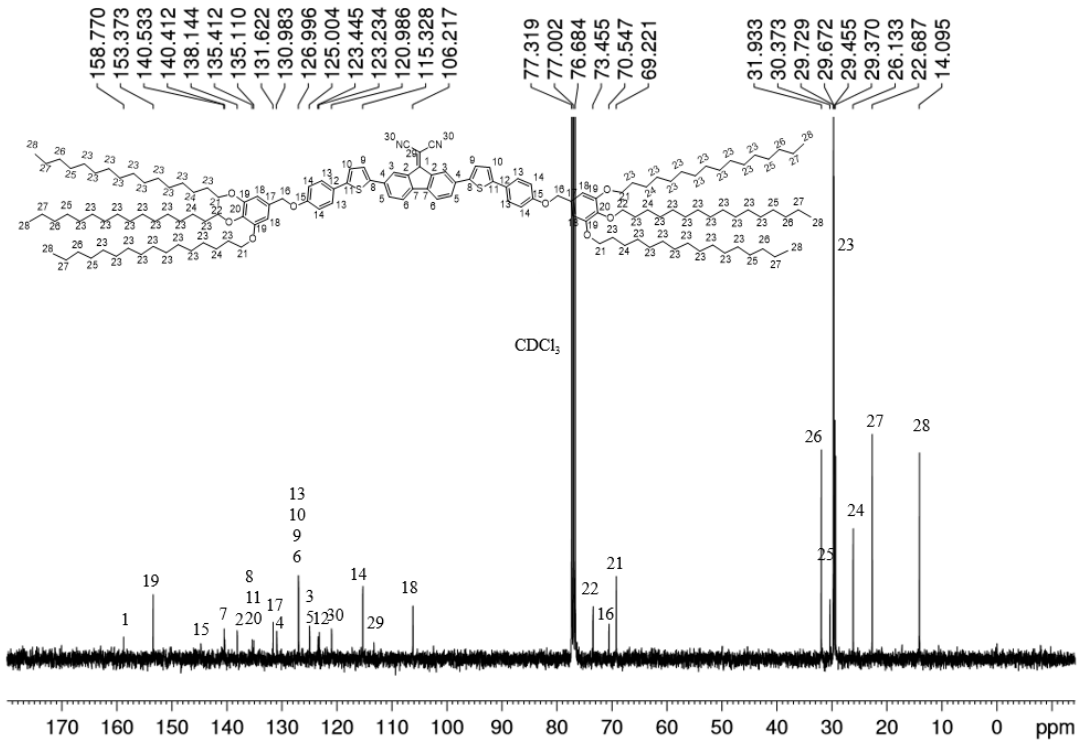

Supplementary Fig. S26 ^{13}C NMR ($CDCl_3$, 100 MHz, ppm) spectra of compound **FCN16.**

S11. Description of the videos

The videos show ED maps and stylized models of $IC^3/12$ and FCN16.

1.1/2.1: ED maps and models of **IC^3/12** (1.1) and **FCN16** (2.1) view along *c*-axis.

1.2/2.2: ED maps (2 cells high) of **IC^3/12** (1.2) and **FCN16** (2.2) at different rotation angles.

1.3/2.3: Models of **IC^3/12** (1.3) and **FCN16** (2.3) at different rotation angles.

References

1. Cheng H. F.*, et al.* Trigonal columnar self-assembly of bent phasmid mesogens. *Chem. Commun.* **54**, 156-159, (2018).
2. Immirzi A., Perini B., Prediction of density in organic crystals, *Acta Crystallogr. A* **33**, 216-218, (1977).
3. Tyler C. A., Morse D. C. Orthorhombic Fddd network in triblock and diblock copolymer melts. *Phys. Rev. Lett.* **94**, 208-302, (2005).
4. Tauc J., Grigorovici R., Vancu A. Optical Properties and Electronic Structure of Amorphous Germanium. *physica status solidi (b)* **15**, 627-637, (1966).
5. Hosticka C., Bose T. K., Sochanski J. S., Generalized treatment of the quadrupole-quadrupole interaction of low symmetry molecules and its effect on the second dielectric virial coefficient, *J. Chem. Phys.* **61**, 2575-2579, (1974).
6. Fontes E., Heiney P. A., Dejeu W. H. Liquid-Crystalline and Helical Order In a Discotic Mesophase. *Phys. Rev. Lett.* **61**, 1202-1205, (1988).
7. Zhao K.*, et al.* Control the self-assembly of fluorenone-based polycatenars by tuning chain length. *Tetrahedron* **75**, 409-415, (2019).
8. Lee T.*, et al.* Synthesis, Structural Characterization, and Unusual Field-Effect Behavior of Organic

Transistor Semiconductor Oligomers: Inferiority of Oxadiazole Compared with Other Electron-Withdrawing Subunits. *J. Am. Chem. Soc.* **131**, 1692-1705, (2009).
9. Fang H.*, et al.* Benzothiadiazole-based D-π-A-π-D fluorophores: Synthesis, self-assembly, thermal and photophysical characterization. *Dyes and Pigments* **147**, 190-198, (2017).